CARBON 78 (2014) 415–427

Available at www.sciencedirect.com

ScienceDirect

journal homepage: www.elsevier.com/locate/carbon

The influence of a hierarchical porous carbon network on the coherent dynamics of a nanoconfined room temperature ionic liquid: A neutron spin echo and atomistic simulation investigation

José Leobardo Bañuelos [a,*], *Guang Feng* [b,*,1], *Pasquale F. Fulvio* [a,2], *Song Li* [b], *Gernot Rother* [a], *Nikolas Arend* [c,3], *Antonio Faraone* [d,e], *Sheng Dai* [a], *Peter T. Cummings* [b], *David J. Wesolowski* [a]

[a] *Chemical Sciences Division, Oak Ridge National Laboratory, Oak Ridge, TN 37831, USA*
[b] *Department of Chemical and Biomolecular Engineering, Vanderbilt University, Nashville, TN 37235, USA*
[c] *Jülich Centre for Neutron Science JCNS, Outstation at the Spallation Neutron Source (SNS), Oak Ridge, TN 37831, USA*
[d] *NIST Center for Neutron Research, National Institute of Standards and Technology, Gaithersburg, MD 20899-6100, USA*
[e] *Department of Materials Science and Engineering, University of Maryland, College Park, MD 20742, USA*

ARTICLE INFO

Article history:
Received 27 January 2014
Accepted 8 July 2014
Available online 15 July 2014

ABSTRACT

The molecular-scale dynamic properties of the room temperature ionic liquid (RTIL) 1-butyl-3-methylimidazolium bis(trifluoromethylsulfonyl)imide, or $[C_4mim^+][Tf_2N^-]$, confined in hierarchical microporous–mesoporous carbon, were investigated using neutron spin echo (NSE) and molecular dynamics (MD) simulations. Both NSE and MD reveal pronounced slowing of the overall collective dynamics, including the presence of an immobilized fraction of RTIL at the pore wall, on the time scales of these approaches. A fraction of the dynamics, corresponding to RTIL inside 0.75 nm micropores located along the mesopore surfaces, are faster than those of RTIL in direct contact with the walls of 5.8 nm and 7.8 nm cylindrical mesopores. This behavior is ascribed to the near-surface confined-ion density fluctuations resulting from the ion–ion and ion–wall interactions between the micropores and mesopores as well as their confinement geometries. Strong micropore–RTIL interactions result in less-coordinated RTIL within the micropores than in the bulk fluid. Increasing temperature from 296 K to 353 K reduces the immobilized RTIL fraction and results in nearly an order of magnitude increase in the RTIL dynamics. The observed interfacial phenomena underscore the importance of tailoring the surface properties of

* *Corresponding authors.*
E-mail addresses: banuelosjl@ornl.gov (J.L. Bañuelos), gfeng@hust.edu.cn (G. Feng).
[1] Present address: State Key Laboratory of Coal Combustion, School of Energy and Power Engineering, Huazhong University of Science and Technology, Wuhan 430074, China.
[2] Present address: Department of Chemistry, University of Puerto Rico, Río Piedras Campus, San Juan 00931, Puerto Rico.
[3] Present address: Jülich Centre for Neutron Science JCNS, Outstation at MLZ, D-85747 Garching, Germany.
http://dx.doi.org/10.1016/j.carbon.2014.07.020

porous carbons to achieve desirable electrolyte dynamic behavior, since this impacts the performance in applications such as electrical energy storage devices.

1. Introduction

Porous carbon materials, in combination with room-temperature ionic liquids (RTILs), have recently emerged as promising materials for use in electrical energy storage devices such as electric double layer capacitors (EDLCs). RTILs have desirable properties such as low volatility, good electrical conductivity, and high thermal and electrochemical stability [1–3]. Most materials used as EDLC electrodes are composed of high surface area carbon particles with internal pores to improve the energy density of EDLCs [4–6]. Because the high surface area of carbons used in EDLCs result from their large volumes of internal micropores and mesopores, compared to small external surface areas, the electrolytes are essentially confined within the carbon particles. Confinement has implications on the density, viscosity, and diffusion of the electrolyte confined in pores compared to the bulk liquid, of great importance for the development of energy storage devices as well as in applications that involve control of the RTIL-solid interface.

Although several studies using various experimental techniques [2] and computational approaches have been undertaken to understand bulk RTIL dynamics, the dynamics of these fluids under conditions of nanoconfinement have not been fully explored. Neutron spin echo (NSE) [7–10] and molecular dynamics (MD) simulations [11] are powerful techniques that can be combined and used to describe bulk and confined RTIL dynamics. To date, MD methods have been used to investigate the dynamics of confined RTILs in model carbon slit-like pores and in cylindrical silica pores [12,13], and experimentally by a combined NMR and MD study of RTILs in cylindrical silica and carbon pores [14]. All of these investigations reported bulk-like dynamics near the center of large mesopores, while the dynamics near the pore surface were much slower.

The behavior of RTIL electrolytes at the complex surfaces of hierarchical porous materials, i.e., carbons, is influenced by surface heterogeneities [14]. While an experimental description of the surface heterogeneities and micropore structures has not been addressed, the dynamics near such complex surfaces cannot be explained using classical theories. Hence, recent work has focused on developing theories to treat RTILs at solid–liquid interfaces [15,16]. Although experimental support for RTIL properties at smooth, planar interfaces continues to grow [17–19], studies of RTILs within complex carbon surfaces have been missing. Such studies have the potential to advance the theoretical efforts. Most importantly, advances in MD simulations could help develop an accurate model to explain the effects of carbon pore size and geometry on the electrochemical performance of carbon-based EDLCs using various electrolytes.

Previously, our small angle X-ray scattering (SAXS) and neutron scattering (SANS) combined with MD studies [20] have demonstrated the greater affinity of RTIL cations for the surfaces of carbon pores within an RTIL monolayer. This study provided a description of the impact of micropore geometry on the structure of confined RTILs, without reference to the confined RTIL dynamics. In this direction, NSE is a powerful tool for studying the dynamic properties of fluids under nanoconfinement [21–26]. It allows measuring the coherent dynamics arising from spatially-correlated groups in the liquid structure. Time-dependence is obtained directly in the normalized coherent intermediate scattering function (CISF), $S(Q, t)/S(Q, 0)$. Depending on a sample's properties and specific instrument configuration, NSE may probe dynamics on time scales of a few picoseconds to several hundred nanoseconds. A predicted CISF can be also be extracted directly from the time-trajectories of individual atoms in an MD simulation, by factoring in their coherent neutron scattering cross sections. Thus, NSE and MD, conducted on similar systems, are ideally suited to both model validation and atomic/molecular interpretation of the scattering from a molecular ensemble. Neutrons are highly penetrating, enabling information to be obtained for the entire sample volume irradiated. Since the matrix in a porous solid is relatively immobile, except for molecular vibrations and lattice phonons, only the pore-filling fluid contributes significantly to changes in the CISF on nanosecond time scales. Furthermore, through selective isotope substitutions, such as D for H, which change the neutron scattering cross sections of specific components of the system, individual species contributions to the CISF can be isolated.

In this paper, NSE and MD simulation studies are used to investigate the dynamics of the RTIL 1-butyl-3-methylimidazolium bis(trifluoromethylsulfonyl)imide ($[C_4mim^+][Tf_2N^-]$) inside hierarchical microporous–mesoporous carbons [6,27]. This study provides molecular-level information of dynamics at an interface and inside micropores, an area that currently lacks sufficient experimental investigation in the EDLC community. The purpose of this study is to study the properties of the interfacial fluid in an electrode material whose hierarchical structure makes it a good supercapacitor material. It is extremely difficult to study an interface if the sublayers far from the surface are still present. By preparing samples in which the degree of filling of the porous substrate is controlled, specific regions of interest were isolated for interrogation by the NSE technique. In this paper, we describe the RTIL dynamics inside of micropores, which are completely filled in our system, as well as the RTIL dynamics at a mesopore interface.

Because the $[C_4mim^+][Tf_2N^-]$ bulk-phase thermophysical [28–30] and structural [31,32] properties have been investigated and optimized potentials have been developed [33,34], its choice provides a solid basis for exploring RTIL properties under pore confinement. Two porous soft-templated carbons with uniform cylindrical mesopores were used: one with

5.8 nm-size mesopores and the other containing both 7.8 nm-size mesopores as well as 0.75 nm slit-shaped micropores (IUPAC defines mesopores as having sizes between 2 nm and 50 nm while micropores have sizes < 2 nm [35]). This class of carbon materials has attracted interest for use as electrodes in EDLCs [6] due to their hierarchical structure of micropores and mesopores that allow fast electron and ion transport. The MD simulations presented herein incorporate validated force fields [36,37] into an analogous physical model (which combines mesopore and micropore effects on RTIL dynamics) and are used to verify and help explain the dynamics measured from NSE.

2. Experimental section

2.1. *Materials synthesis and preparation*

The complete sample synthesis and preparation methods, as well as structural characterization by nitrogen adsorption and small angle X-ray scattering (SAXS) analysis, for the current system are discussed in detail in our previous work [20]. A summary is provided below. The mesoporous carbon (MC) was synthesized using a soft-templating synthesis method [27,38]. This consisted of the self-assembly of resorcinol (Sigma–Aldrich, 99%) and formaldehyde (Sigma–Aldrich, 37 wt.%) in the presence of triblock copolymer Pluronic F127 (EO_{106}-PO_{70}-EO_{106}, BASF) for the 7.8 nm mesoporous carbon (labeled MC-127), and Pluronic F87 for the 5.8 nm mesoporous carbon (labeled MC-87), and purchased from Sigma–Aldrich according to previously reported recipes [38–39]. C_4mim.Tf_2N-D_{15} was prepared from C_4mim.Br-D_{15} (Isotec Stable Isotopes) via a modified anion exchange procedure [40] using lithium bis(trifluoromethylsulfonyl)imide (3M) in D_2O instead of H_2O. To prepare the ionic liquid-MC composites calculated amounts of RTIL corresponding to the different pore loadings were mixed with deuterated methanol-D_4 (Alfa Aesar, 99.8% isotopic). Because one goal is to study pure RTIL in confinement, the initial solvent was intentionally evaporated leaving behind only RTIL. Samples were mixed and dried at high temperature and under vacuum using a protocol described elsewhere [20]. Prior to loading into measurement cells, the samples were placed under vacuum for at least 24 h at 80 °C. All samples were loaded into measurement cells under an argon atmosphere.

Nitrogen adsorption isotherms were measured for the empty porous carbons as well as the RTIL-carbon nanocomposite samples. The pore size, total pore volume, and micropore volume obtained from N_2 adsorption analysis are given in Table 1. Small angle X-ray scattering (SAXS) data analysis [20] of the empty MC-127 yielded slit-shaped micropores with a size of 0.75 nm for micropore morphology and size. We do not specify a depth for several reasons. First the observed phenomena highly depend on the width and total surface area in contact with the RTIL. Second, in the real system, the micropores that form during the carbonization process vary in the depth to which they permeate the mesopore walls, and in some cases may even form interconnections with adjacent mesopores. In this system, it is difficult to determine the depth of the slit-pores using gas adsorption and small angle scattering techniques. For this reason, we define the system in terms of the values given in Table 1, and the corresponding micropore to mesopore ratios. The micropore–mesopore in the MD model is constructed in a similar way as described in the modeling setup section below. The RTIL total pore volume filling fraction, v_f, shown in Table 1 was obtained from SAXS analysis of RTIL-carbon nanocomposite samples, labeled S_1, S_2, and S_3. For example, $v_f = 0.5$ for sample S_3 corresponds to half of the total carbon pore volume being filled with RTIL. One unexpected finding during the preparation of the experimental system was the degree of densification [20] in the micropores (the original experiment was designed to measure samples with more evenly-spaced filling amounts assuming bulk density, including a completely filled sample; $v_f = 1$, however, was not measured in this study). Nevertheless a good representation of micropore-filled, and two mesopore surface coverages was still achieved.

We demonstrated that most of the RTIL in sample S_1 is contained in the micropores of the mesoporous carbon and that subsequent filling of the pore volume in samples S_2 and S_3 takes place in the mesopores of MC-127 [20]. Carbon, hydrogen, nitrogen (CHN) elemental analysis by combustion was carried out to obtain an accurate estimate of the RTIL/MC-127 composition for samples S_1, S_2, and S_3 and the resulting mass fractions are shown in Table 1 (column e). The changes in the scattering data agree with the expected compositional changes in the carbon particle as the micropore/mesopores filled with RTIL, indicating that the RTIL was found inside the pores, and at a high density (Table 1, column f), as

Table 1 – Empty mesoporous carbon and RTIL/MC-127 structural parameters obtained from N_2 adsorption, SAXS, and CHN elemental analysis.

Sample	[a] Pore size (nm)	[b] V_{total} (cm^3/g)	[c] V_{micro} (cm^3/g)	Sample	[d] v_f	[e] RTIL/MC-127 (g/g)	[f] ρ_{pore}/ρ_{bulk}
MC-87	5.8	0.46	0.12	S_1	0.08	0.180	3.55
MC-127	7.8	0.53	0.045	S_2	0.2	0.256	2.19
				S_3	0.5	0.355	1.4

[a] Pore width calculated according to the improved KJS method [41,42] using statistical film thickness for nonporous reference carbon material.
[b] Single point pore volume from adsorption isotherms at relative pressure $p/p_0 \approx 0.98$.
[c] Micropore volume calculated in the α_s-plot [43] range of 0.75–1.00.
[d] RTIL total pore volume filling ratio.
[e] RTIL mesoporous carbon composite mass ratios obtained from CHN analysis.
[f] Experimentally-obtained [20] ratio of RTIL density in pores to the bulk state.

opposed to the outer surface or intergrain macrospaces of the carbon powder.

2.2. Small angle neutron scattering

Small angle neutron scattering (SANS) measurements of the fully deuterated RTIL were conducted at BL-6B (EQ-SANS), Spallation Neutron Source (SNS), Oak Ridge National Laboratory (ORNL). SANS intensity as a function of momentum transfer, Q, was collected (Q is related to the d-spacing (d), scattering angle (2θ), and radiation wavelength (λ), by the relation: $Q = 2\pi/d = 4\pi\sin(\theta)/\lambda$). The SANS data for the deuterated ionic liquid was placed on an absolute scale using two methods: (1) By using a standard reference sample (Vycor) and (2) by enforcing the extrapolated forward scattering to the isothermal compressibility limit with the expression resulting from kinetic and fluctuation theory [44,45] $S(0) = k_B T\rho_N\chi_T$, where k_B is Boltzmann's constant, T is the absolute temperature, ρ_N is the molecule number density, and χ_T is the isothermal compressibility. We used $\chi_T = 0.526\ \text{GPa}^{-1}$ at room temperature from references [34,46]. Both methods yielded similar normalized scattering curves.

2.3. Neutron spin echo experiment

The neutron spin echo experiment carried out at the NIST Center for Neutron Research (NCNR) was performed using the spectrometer located at the end position of NG-5. The incoming neutron wavelength was set to 5 Å using a velocity selector, with a $\Delta\lambda/\lambda \approx 20\%$. In this configuration the instrument can achieve a maximum Fourier time of 10.0 ns, however, due to limited beam time allocated, the measurements were performed up to a maximum of 1 ns. Polarized diffraction measurements were carried out at the beginning of the experiment for the bulk ionic liquid and the mesoporous carbon imbibed with RTIL to determine their relative scattering strengths and choose a Q value where the liquid to carbon coherent signal ratio would be high. The background scattering was subtracted after proper normalization for the volume fraction and transmission factors (to account for self-shielding). A measurement performed on the bulk glassy ionic liquid at 10 K, where the dynamics in the nanosecond timescale are frozen, was used as the experimentally determined instrument resolution. The DAVE software package [47] was used to reduce the NIST NSE data.

A second NSE experiment was performed on the NSE spectrometer (BL-15) at the SNS, ORNL. Since the SNS NSE instrument is contained in a magnetically shielded, wedge-shaped instrument hall [48], measurements were carried out in the long instrument configuration to allow the secondary flight path to rotate to large angles and allow measurements at high Q values; measurements were carried out with a 4.1–6.5 Å wavelength band and at two positions corresponding to average Q's of 0.76 Å^{-1} and 1.4 Å^{-1}. A TiZr calibration standard was used as the experimentally-determined instrument resolution. Measurements were performed using both the "shorty" and standard configuration to cover the 0.002–16 ns range. Since the SNS NSE is a time-of-flight (TOF) instrument, it is possible to bin the data into shorter Q-bins and obtain decay time as a function of Q.

2.4. Modeling setup

Before the confined RTILs were simulated, we performed MD simulations of bulk [C_4mim^+][Tf_2N^-]) in the isobaric–isothermal ensemble at a pressure of 1 atm and temperatures of 275 K, 300 K and 350 K. The obtained bulk properties of RTILs provided a baseline for the setup of the simulation of RTILs inside micropores and mesopores. The mesopore (Fig. 1) was modeled by three-layer concentric carbon nanotubes (CNTs) with a 0.341 nm gap between neighboring walls and an inner diameter that matched the experimentally obtained mesopore diameter. The micropore (see zoomed image in Fig. 1) was modeled by a slit of two walls separated by a 0.75 nm distance and each wall was modeled by a three-layer graphene sheet also with a 0.341 nm gap between neighboring graphene layers. The CNT-made mesopore is 6.1 nm in length and the slit-shaped micropore has a length of 6.1 nm.

To obtain the right number of ion pairs inside the mesopore, the modeled cylindrical pore was connected to an RTIL reservoir of ≈6.6 nm in thickness that allowed the ions to freely enter or leave the mesopore. Then, only the RTIL ion pairs inside the pore were statistically counted in an equilibrium simulation system. Note that to get rid of edge effects from the connection between pore and reservoir, a 1.0 nm-long pore entrance was excluded when counting the ion pairs. Then, the reservoir was removed to leave a simplified system containing the CNTs and RTIL inside, and the periodic boundary condition was applied in the direction along the CNT axis (i.e., the cylindrical mesopore was infinitely long in theory). This simplification of the mesopore system by removing the RTIL reservoir helped save considerable computational resources. For example, at 300 K, the system with an RTIL reservoir has 1204 ion pairs while there are only 294 ion pairs in the simplified MD system consisting of a cylindrical mesopore with a diameter of 5.8 nm and length of 6.1 nm. Similarly, the slit-shaped micropore was also connected to a reservoir of ≈8.0 nm in thickness. In this case, at 300 K, there

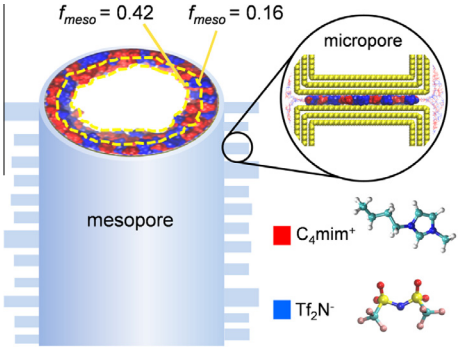

Fig. 1 – Schematic of the mesoporous–microporous system. The mesopore filling fractions v_{meso} = 0.16 and 0.42, denoted by the dashed line, were used to calculate $S_{2,meso}$ and $S_{3,meso}$, while filled RTIL–micropores (zoomed image) were used to obtain S_{micro}. The total ion density and relative number of RTIL ions in mesopores compared to in micropores were calibrated using the results of our previous structural investigation [20].

are about 186 ion pairs in the RTIL reservoir compared to about 24 ion pairs inside the 0.75 nm-sized micropore (excluding the 1.0 nm-long entrance). The different mesopore loading fractions v_{meso}, were determined by removing the number of ions with respect to the total number of ions in the full loading case in order to achieve the same mass fraction as in the experimental system. For example, the number of ion pairs in the pore loading of 16% and 42% is 47 and 123, respectively. Further details of the simulation setup are provided in our previous work [20]. The MD-obtained composite CISFs, $S_{n,MD}$ shown in Fig. 3, were obtained from the RTIL mass-normalized linear combination of MD-obtained RTIL dynamics in the micropores and mesopores. MD simulations were carried out on micropores completely filled with RTIL and at mesopore filling fractions, v_{meso}, of 0.16 and 0.42, and CISFs S_{micro}, $S_{2,meso}$, and $S_{3,meso}$ were obtained, respectively.

3. Results and discussion

3.1. *Experiment 1: Full pore filling*

Two separate neutron spin echo experiments were carried out. In the first experiment, bulk alkyl chain-deuterated [C_4mim^+][Tf_2N^-], and the same liquid confined in 5.8 nm pores, herein referred to as IL_{alkyl} and MC5.8-IL_{alkyl}, respectively, were measured at the NIST NSE spectrometer [49]. In order to distinguish the geometric confinement effects from those of the carbon surface on the RTIL dynamic properties, the second NSE experiment probed RTIL dynamics as a function of pore volume filling fraction v_f inside 7.8 nm pores. Fully deuterated [C_4mim^+][Tf_2N^-], herein referred to as IL_{deut}, was used and the measurements were carried out at the SNS NSE spectrometer [48]. To the best of our knowledge, this is the first study to use NSE to probe the dynamics of an ionic liquid confined in a hierarchical porous carbon.

The diffraction profiles of IL_{deut} (measured on SNS BL-6B [50]) and MC5.8-IL_{alkyl} are shown in Fig. 2a. The bulk structure shows two broad peaks near 0.8 $Å^{-1}$ and 1.4 $Å^{-1}$; these features have been discussed previously [32,51]. Low-Q scattering from the pore structure of the MC5.8-IL_{alkyl} composite for $Q < 1$ $Å^{-1}$ (Fig. 2a) introduced a high background signal that made NSE measurements at 0.8 $Å^{-1}$ unfeasible during this experiment's beam time. NSE measurements were carried out on IL_{alkyl} at 275 K and MC5.8-IL_{alkyl} at 275 K and 300 K, each at $Q = 1.4$ $Å^{-1}$ (Fig. 2b). The CISF of IL_{deut} collected at 296 K is also shown in Fig. 2b. The bulk dynamics were fit with the expression

$$S_{RTIL} = fe^{-\left(\frac{t}{\tau}\right)^{\beta}} \quad (1)$$

Fits of Eq. (1) for the bulk RTILs are shown in Fig. 2b. A short-time decay component faster than the minimum observation time, t_{min}, is present and results in a measured S_{RTIL} at t_{min} that is less than unity. The origin of the fast relaxation process cannot be identified with certainty solely on the basis of the available data. However, it could arise from fast conformational changes, e.g. of the alkyl chains, and motions within the first neighbors shell which are sufficient to partially reduce the correlation between the structures originating the coherent signal. These dynamical processes do not involve movements large enough, compared to the experimental observation scale (≈1/Q), to cause the CISF to decay to zero. The motions in the fast relaxation process are also likely correlated with single-particle ballistic and sub-diffusive dynamic regimes [12,52–54], since these depend on the distance to nearest neighbor molecules and occur on similar time scales. The stretching exponent, $\beta = 0.59$, obtained from fitting Eq. (1) to the RTIL data at 275 K and 296 K, is indicative of dynamics that involve more than one decay component in the primary relaxation time scale τ. At $Q = 1.4$ $Å^{-1}$, β encapsulates the complex interactions between the cation head groups, alkyl chains, and anions, and provides an average decay time $\langle\tau\rangle$. The mean relaxation time $\langle\tau\rangle$ is given by $\tau = \frac{\tau}{\beta}\Gamma\left(\frac{1}{\beta}\right)$, where $\Gamma\left(\frac{1}{\beta}\right) = \int_0^\infty x^{\left(\frac{1}{\beta}-1\right)}e^{-x}dx$. The $\langle\tau\rangle$ from fits of the bulk data in Fig. 2c are given in Fig. 3c and discussed later.

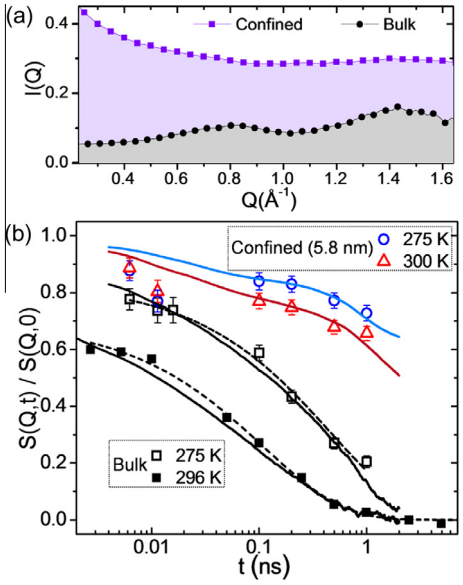

Fig. 2 – (a) Diffraction measurement of IL_{deut} and MC5.8-IL_{alkyl} showing the bulk RTIL structural peaks and high background at low-Q, respectively. (b) Coherent intermediate scattering functions obtained from NSE (symbols) and MD (solid lines) for alkyl chain-deuterated bulk [C_4mim^+][Tf_2N^-] (IL_{alkyl}) at 275 K, fully deuterated RTIL (IL_{deut}) at 296 K and IL_{alkyl} confined in 5.8 nm carbon pores (MC5.8-IL_{alkyl}) at 275 K and 300 K. All CISFs were collected at $Q = 1.4$ $Å^{-1}$. The dashed lines are fits to the data using the expression for S_{RTIL} given in Eq. (1). Here and throughout the paper, error bars represent one standard deviation. (A color version of this figure can be viewed online.)

The confined RTIL CISFs shown in Fig. 2 may be described in terms of three components: (1) the bulk-like RTIL dynamics, S_{RTIL}, (2) a slow, pore surface-immobilized RTIL component, $S_{immob}(Q, t)$, and (3) a constant elastic background due to the carbon matrix, $F_c(Q)$. The experimental CISF was fit with the function,

$$S_{RTIL+C} = S_{RTIL} + B \quad (2)$$

with S_{RTIL} given by Eq. (1) and B given by $B = S_{immob}(Q, t) + F_c(Q)$. The $S_{immob}(Q, t)$ describes dynamics more than an

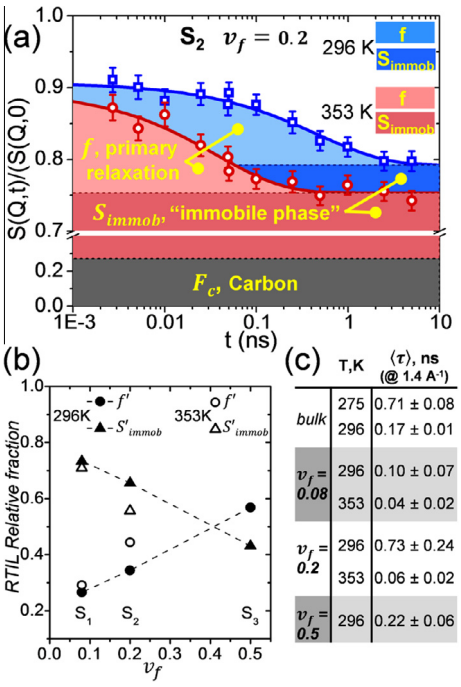

Fig. 3 – (a) Coherent intermediate scattering functions (CISFs) for S_2 at 296 K and 353 K. NSE data is shown along with the fit of Eq. (2) with individual dynamic components highlighted. (b) Plot of RTIL dynamic components f' and S'_{immob} vs. pore-filling fraction v_f at 296 K, and 353 K for samples S_1, S_2, and S_3. The dashed lines are guides to the eye. (c) NSE mean relaxation times $\langle\tau\rangle$ obtained at Q = 1.4 Å^{-1} for the bulk RTIL and at loadings (v_f) of 0.08, 0.2 and 0.5.

order of magnitude slower than the bulk-like dynamics. Such dynamics generally lay beyond the time window accessible in the current experiments and therefore appear as effectively immobile components to the present experiment.

The MD-obtained CISFs for the bulk, $S_{RTIL,MD}$, and the RTIL/carbon composite, $S_{RTIL+C,MD}$, are shown in Fig. 2, and a simulation snapshot is shown in Fig. 2b. Similar to the experimental CISF, $S_{RTIL+C,MD}$ is given by $S_{RTIL+C,MD} = S_{5.8,MD} + B$. Here, $S_{5.8,MD}$ is the simulated CISF of RTIL confined in 5.8 nm pores. Full relaxation of the RTIL dynamics should result in a CISF which decays to a constant value, or plateau, corresponding to the carbon elastic background $F_c(Q)$ at high Fourier times. Our observations, on the other hand, reveal the presence of a component with long decays beyond the maximum measurement time, t_{max}, of the current experiment. Thus, the RTIL plateau region is not well-resolved and B is treated as a constant. For comparison, water confined in vermiculite clay decays to a plateau by 1 ns at 303 K, and at 280 K still shows a decay in the self-intermediate scattering function even at 2 ns [22]. Thus, it is reasonable to expect that the more viscous RTIL fluid will decay over longer times near surfaces. Indeed, increasing the temperature from 275 K to 300 K caused a faster decay in the CISF of the confined RTIL: B decreased from 0.4 to 0.25. The decrease in B shows that the $S_{immob}(Q, t)$ component of the long Fourier time signal is due to RTIL dynamics whose full relaxation occurs beyond t_{max}. Analysis of higher temperature (353 K) data in the second experiment, discussed later, estimates $S_{immob}(Q, t)$ to be on the 100-ns time scale.

3.2. *Experiment 2: Partial pore filling*

In the second NSE experiment, the influence of the pore surface morphology on the RTIL dynamics was investigated in more detail by carrying out measurements as a function of IL_{deut} total pore volume filling fraction (v_f). The porous carbon consists of 7.8 nm cylindrical mesopores and 0.75 nm slit-like micropores which comprise 8.5% of the total pore volume and decorate the mesopore surfaces. Samples labeled as S_1, S_2, and S_3, corresponding to v_f's of 0.08, 0.2, and 0.5, respectively, were all measured at (296 ± 0.1) K, and at (353 ± 0.2) K for samples S_1 and S_2. Most of the IL_{deut} in sample S_1 is located inside the micropores and along the mesopore walls. One advantage of this approach is the ability to experimentally delineate the dynamics near the mesopore center, where bulk-like dynamics are found, from the dynamics at the complex surface. The sample preparation and structural analysis are described in detail in our previous work [20]. Higher Fourier times than in the first experiment were accessible due to higher counting statistics and the use of a fully deuterated RTIL.

The confined RTIL CISFs were fit with Eq. (2) with $S_{immob}(Q, t)$ treated as a constant S_{immob}. We now consider the relative contribution of each confined RTIL component, namely f (the amplitude of the primary component given in Eq. (1)) and S_{immob}, on the CISF. Fig. 3a shows the fit of Eq. (2) to sample S_2 NSE data and highlights the contribution of each S_{RTIL+C} component at 296 K and 353 K. At 296 K, the primary relaxation contains a fast decay component that occurs primarily at $t < t_{min}$. As temperature is increased to 353 K, the fast decay occurs completely outside the experiment's time window resulting in a lower CISF value at t_{min}. As the temperature is raised from 296 K to 353 K, t clearly shifts to lower decay times (Fig. 3c). The S_{immob} dynamics at 296 K are too slow for an estimate of the time scale. However, if at 353 K the immobile component is explicitly defined as $S_{immob}(Q,t) = f_{immob}e^{-(t/\tau_{immob})}$, a time constant $\tau_{immob} = 130 \pm 50$ ns for samples S_1 and S_2 can be estimated by fitting Eq. (2) to the NSE data; the significant error is due to the measurement's cut-off at long times.

All NSE data in Fig. 4 were fit with Eq. (2). The relative contributions of the RTIL dynamic components f and S_{immob}, as v_f and temperature are varied, are shown in Fig. 3b, where $f' = f/(f + S_{immob})$ and $S'_{immob} = S_{immob}/(f + S_{immob})$. Fig. 3a and b show that a fraction of the RTIL is released from the immobile phase (S_{immob}) and contributes to the dynamics of the bulk-like phase (f), noted by the decrease in S_{immob} and increase in f for sample S_2. A similar trend is found for S_1 (Fig. 3b, Fig. 4). The changes in the RTIL primary relaxation (f component), and in the surface-immobilized RTIL dynamics (S_{immob} component), share an inverse relationship as a function of pore filling, i.e., at low loading, most RTIL dynamics are due to RTIL-pore wall interactions, whereas at high loadings a larger fraction of the dynamics exhibit bulk-like behavior.

The MD simulations are able to reproduce the CISFs of the confined ionic liquid, $S_{n,MD}$ as a function of v_f (n = 1–3 for each sample) and temperature. The CISFs were calculated by the

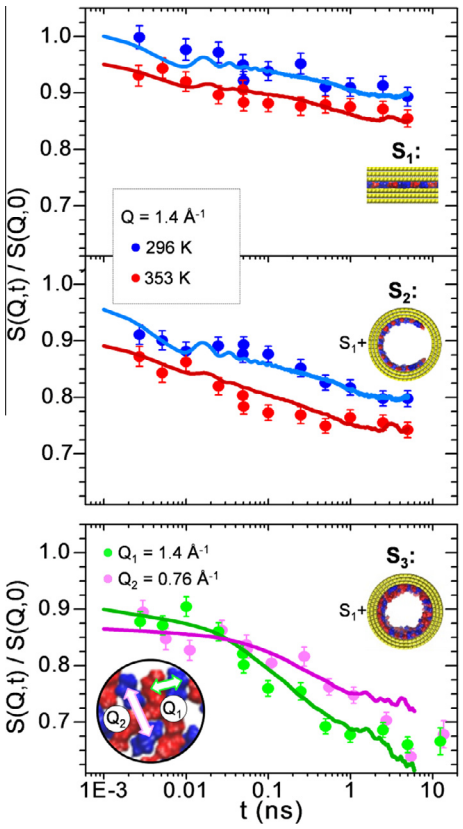

Fig. 4 – CISFs for fully deuterated RTIL samples S_1, S_2, and S_3 confined in microporous–mesoporous carbon (7.8 nm mesopores). Samples S_1 and S_2 were measured at Q = 1.4 Å^{-1} and at 296 K and 353 K (top two plots). Sample S_3 was measured at 296 K and at 0.76 Å^{-1} and 1.4 Å^{-1}(bottom plot). Experimental values are indicated by symbols and simulation results ($S_{n,MD}$) with solid lines. An overall slowing of interparticle dynamics is found in the confined samples. The insets on the right-hand-side are snapshots of the simulations used to generate the CISFs. The left inset in the bottom plot shows the length scale of the fluctuations probed at the two measured Q-values; cations are shown in red and anions in blue.

software nMOLDYN [55] based on MD-obtained trajectories. The $S_{n,MD}$ shown in Fig. 4 are the RTIL mass-normalized linear combination of CISFs in the micropores and mesopores. To simplify the simulation system, the dynamics in the micropores and in the mesopores were modeled separately. Simulations of completely filled 7.5 Å slit-like micropores and of cylindrical mesopores partially filled with RTIL were carried out to obtain S_{micro}, $S_{2,meso}$ and $S_{3,meso}$, respectively. Additional details are contained in the Experimental Section. The CISFs were combined to obtain $S_{n,MD}$ as follows: $S_{n,MD} = m'_{micro}S_{micro} + m'_{n,meso}S_{n,meso} + F'_{n,c}$, normalized such that the total mass $m'_{micro} + m'_{n,meso} = 1$. For $n = 1$, the expression simplifies to $S_{1,MD} = S_{micro} + F'_{n,c}$. At the lower loadings (S_1 and S_2), small amplitude oscillations with a period of ≈0.018 ns are present in the simulated CISFs due to the lower averaging statistics from the micropore component. The micropore/mesopore mass fractions of each $S_{n,MD}$ plotted in Fig. 4 were chosen to match the experimental mass fractions in order to give the proper weight to the CISF components and adequately represent the composite CISFs. Diffraction data was used to obtain the background term, F'_c at Q = 1.4 Å^{-1} in the modeled CISFs.

The relation of the RTIL dynamics with diffusion-type processes was investigated by analyzing the dependence of the inverse of the characteristic decay time $1/\langle\tau\rangle$ with Q. The IL_{deut} and S_3 SNS NSE data were collected with enough statistics to allow re-binning the data by neutron time-of-flight and provide a Q-range of 0.685–1.603 Å^{-1}. A linear dependence in a $1/\langle\tau\rangle$ vs. Q^2 plot is indicative of simple diffusion, i.e.,

$$1/\langle\tau\rangle = D_{eff}Q^2, \quad (3)$$

and the slope of the line gives the effective diffusion coefficient. For the bulk liquid, the decay times follow this behavior, yet a subtle de Gennes narrowing [56] (i.e., slower decay times in the Q region corresponding a liquid's structural peak) is observed near the low-Q peak (Fig. 5). A fit of Eq. (3) over the full Q-range for the bulk gives $D_{eff} = (2.56 \pm 0.17) \cdot 10^{-11}$ m^2/s (Fig. 5), which is close to the published C_4mim^+ NMR diffusion value [14] of $(2.5 \pm 0.2) \cdot 10^{-11}$ m^2/s and $(2.3 \pm 0.2) \cdot 10^{-11}$ m^2/s from the current MD simulations. The effective diffusion coefficients for IL_{deut} and S_3 were calculated by fitting Eq. (3) to $\langle\tau\rangle$ values obtained near the first structural peak at Q = 0.76 Å^{-1} and near the second peak at Q = 1.4 Å^{-1} (Fig. 5). $D_{low\text{-}Q}$, obtained near Q = 0.76 Å^{-1}, corresponds primarily to long-range cation–cation, chain–chain, and anion–anion fluctuations, whereas $D_{high\text{-}Q}$, obtained near 1.4 Å^{-1}, corresponds primarily to short-range to cation–anion, cation–cation, and

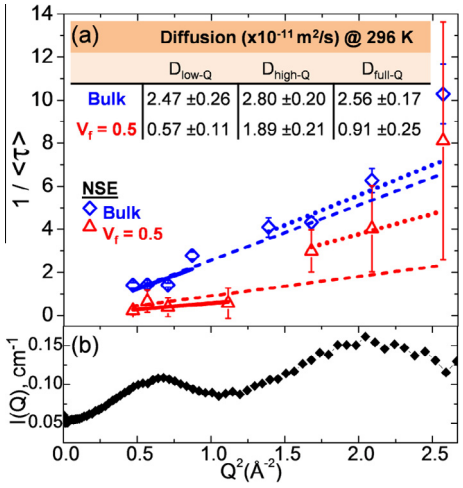

Fig. 5 – The slope of the $1/\langle\tau\rangle$ vs. Q^2 plot gives the effective diffusion coefficient. (a) (◇) Bulk and (△) S_3 sample data collected at 296 K on the SNS NSE spectrometer. Dashed lines: Fit of diffusion equation using all data points. Solid lines: Fit using low-Q decay data. Dotted line: Fit using high-Q decay data. The diffusion coefficients obtained from each of the fits is shown in the inset. (b) Scattering profile for the deuterated bulk RTIL. Slight de Gennes narrowing is observed from comparison of $1/\langle\tau\rangle$ with the structural peak positions. (A color version of this figure can be viewed online.)

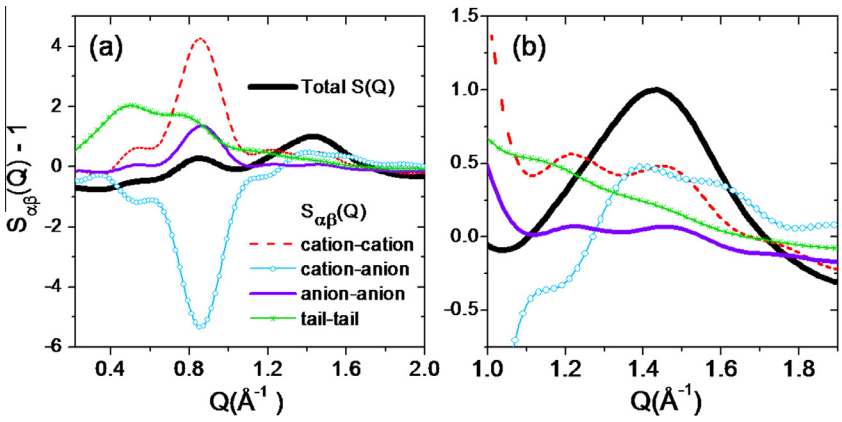

Fig. 6 – (a) The total and partial neutron-weighed bulk RTIL structure factors, S(Q) and $S_{\alpha\beta}(Q)$, in the S(Q) − 1 representation. The modeled total S(Q) is very similar to the measured curve in Fig. 2a (b) Close-up of the structure factors near the 1.4 Å^{-1} peak where most NSE measurements were conducted. The plot shows that the cation–anion and the cation–cation $S_{\alpha\beta}(Q)$ contribute the most to the peak at 1.4 Å^{-1}, followed by the tail–tail $S_{\alpha\beta}(Q)$ and very little for the anion–anion $S_{\alpha\beta}(Q)$. (A color version of this figure can be viewed online.)

chain–chain fluctuations [2,51,57]. Fig. 6 shows the total and partial neutron-weighted bulk RTIL structure factors which illustrate the RTIL structural components responsible for the observed dynamics. The similar slope in the $1/\langle\tau\rangle$ vs. Q^2 plot near Q = 1.4 Å^{-1}, for the bulk and S_3 samples indicates small sensitivity of $\langle\tau\rangle$ to confinement; $D_{\text{high-Q}}$ slows to 68% of the bulk value with confinement. The dynamics, however, are more sensitive to confinement at lower Q, and $D_{\text{low-Q}}$ decreases to 23% of the bulk value. Although the intensity I(Q) of the Q = 1.4 Å^{-1} peak is higher than the Q = 0.76 Å^{-1} peak, de Gennes narrowing is not visible and the higher diffusion values at high-Q suggest that other motions accelerate the high-Q dynamics.

The observed behavior is described as follows. At high-Q, the signal is primarily due to nearest-neighbor anion–cation correlations and results from the cumulative effect of only the nearest neighbors (Fig. 6) resulting in S_3 dynamics at high-Q which resemble those of the bulk liquid. At lower Q, the dynamics result from the cumulative effect of interactions with a larger number of constituents over larger length scales [57]. Such length scales begin to approach the size of the confinement and are therefore more easily perturbed by nanoconfinement. A molecular dynamics simulation of $[C_4mim^+][Tf_2N^-]$ [30] shows that the self-intermediate scattering function decays faster than the CISF at similar Q. This supports our observation that the collective motions in both Q-regions are not entirely of a diffusive nature, but instead are coupled with other types of motions.

We previously mentioned that some of the measured dynamics are likely correlated with ballistic and sub-diffusive dynamic regimes since these also occur at time and length scales similar to that probed in this experiment. These regimes and their connection with the confined RTIL must be considered. The motion of an ion at short distances before it senses its neighbors is known as the ballistic regime, occurring in the first few picoseconds, and has faster dynamics than the other regimes. Next, the dynamics slow down due to the ions being temporarily trapped in cages formed by neighboring molecules; this is known as the subdiffusive regime. At longer times, as the ions escape the molecular cages in which they are found, the ions transition to the diffusive regime [12]. The slope of the mean squared displacement (MSD) vs. time plot should be linear and may be used to calculate the diffusion coefficient in this regime. The one-dimensional MSD vs. time in the range of 1–3 ns, for example as shown in Fig. 7b, was used to calculate the diffusion coefficients (Fig. 7c) of all the simulated systems.

The $\langle\tau\rangle$ values in Fig. 3c, show longer decay times for the confined samples compared to the bulk at 296 K. Interestingly, the $\langle\tau\rangle$ decay for S_1 is faster than for S_2. In comparison, the diffusion coefficients of the individually MD modeled components in Fig. 7c, i.e., RTIL in the bulk phase, in micropores, and in mesopores, show that the dynamic component of RTIL inside the micropores is faster than RTIL interacting with the mesopore walls, yet still lower than the bulk liquid. This follows the trend observed for the $\langle\tau\rangle$ values. The MD-derived diffusion coefficients (Fig. 7c) show that at 16% mesopore loading, the average diffusion is slower than at 42% mesopore loading due to the higher fraction of RTIL near the wall. However, the diffusion coefficient of RTIL in the micropores is higher than in the partially filled mesopores. Diffusion values from MD calculated at 300 K and 350 K are shown for the bulk RTIL and each confinement simulation in Fig. 7c.

Comparison of $S_{3,\text{meso}}$ with S_{micro} shows that S_{micro} initially decays faster but has a long decay component that is slower than that of $S_{3,\text{meso}}$ (Fig. 7a). The CISF at the minimum time for the micropore begins at a lower level than the mesopore CISF, which means there are molecular rearrangements occurring at faster time scales than the resolution of the simulation. If these motions were captured, both the micropore and mesopore CISFs would begin at S(Q, t)/S(Q, 0) = 1. The CISFs decay across the time window yet do not decay to zero at the highest calculated times in either case. This means there is a component in the RTIL dynamics that extends well beyond the maximum time of the simulation and is not adequately represented. To help find the source of the slow

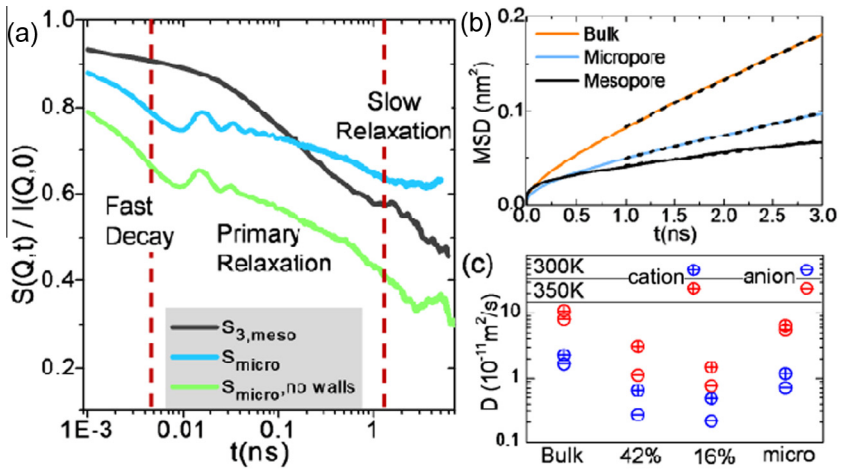

Fig. 7 – (a) CISFs of RTIL inside micropores at 296 K with (blue) and without (green) the RTIL–wall interactions present. $S_{3,meso}$ (black) is shown for comparison. (b) One-dimensional (parallel to the pore wall) mean square displacement (MSD) vs. time plot of bulk RTIL and RTIL in a micropore and mesopore (υ_{meso} = 0.42) at 296 K. The dotted lines indicate the range over which the diffusion was calculated. (c) Comparison of RTIL diffusion coefficients. Values shown are MD results for the bulk, mesopore (42% and 16% loadings), and micropore (full loading), at two different temperatures.

relaxation, the micropore CISF was calculated without the RTIL–wall interactions and $S_{micro,no\ walls}$ was obtained, which includes only confined RTIL–RTIL interactions in the micropore. The dynamics of $S_{micro,no\ walls}$, occurring predominantly along the plane of the slit pore, shows dynamics that decay faster than the total S_{micro} and $S_{3,meso}$ (Fig. 7a). $S_{micro,no\ walls}$ provides a glimpse that the slow relaxation is primarily associated with the RTIL–wall interactions, but even in this case the CISF does not decay to zero, though it does decay to a value lower than $S_{3,meso}$.

The differences between the 3 curves may be explained by considering that a higher fraction of RTIL is in contact with the pore walls in the micropore case than in the mesopore case, and that as a consequence a higher fraction of the RTIL dynamics in the S_{micro} CISF will correspond to RTIL–wall interactions. If the RTIL–wall interactions are removed, then the simulated $S_{micro,no\ walls}$ decays faster in the micropore case. Also, comparison of the experimental tabulated $\langle\tau\rangle$ in Fig. 3c, shows that the primary relaxation component of the CISF decays faster in the micropore case. Fig. 7(a–c) emphasizes that the collective motions of the RTIL are complex and information over longer and shorter time scales, as well as over a wider temperature range, are necessary to observe how/to what extent the dynamics represented by the CISF couple with diffusion. Based on the current information, the diffusion calculated from the selected region in the MSD plot does not account for the slow relaxation due to RTIL–wall interactions, though it does show some correlation with the $\langle\tau\rangle$ of the primary relaxation component. We attribute this behavior to the resulting nearest neighbor-scale local structure of the confined RTIL both along perpendicular and parallel paths to the pore wall as discussed below in the following paragraph.

To shed light on the dynamics that depend on the organization of nearest neighbor molecules, the structure of ions within the modeled micropore and mesopore was explored

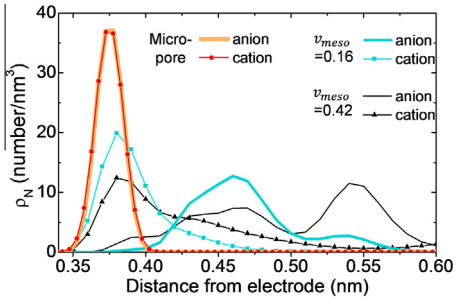

Fig. 8 – (a) Ion density distributions for each MD-modeled component. The alternating cation–anion structure is clearly in the mesopore case, with less overlap in the layering and higher local density in the υ_{meso} = 0.16 case, indicating a more rigid ordered structure than υ_{meso} = 0.42. In the micropores, only a monolayer forms in the narrow pore such that the ions in the two-dimensional ion distribution are equidistant from the pore walls in the direction perpendicular to the walls. (A color version of this figure can be viewed online.)

both perpendicular to and along the pore walls. Fig. 8 shows the RTIL cation and anion density for each of the three modeled systems as a function of the distance from the pore wall. Only a high density monolayer of RTIL may be accommodated within the slit micropore. In this case, both cations and anions are found to be equidistant from the pore walls. Within the mesopore, the RTIL adopts an alternating layered structure with cations found in the innermost layer. The ordering perpendicular to the surface is stronger in the υ_{meso} = 0.16 case than the υ_{meso} = 0.42 case. This is due to the strong influence of the pore wall on the RTIL structure at low loading. As more RTIL is added, the bulk-like fluid helps

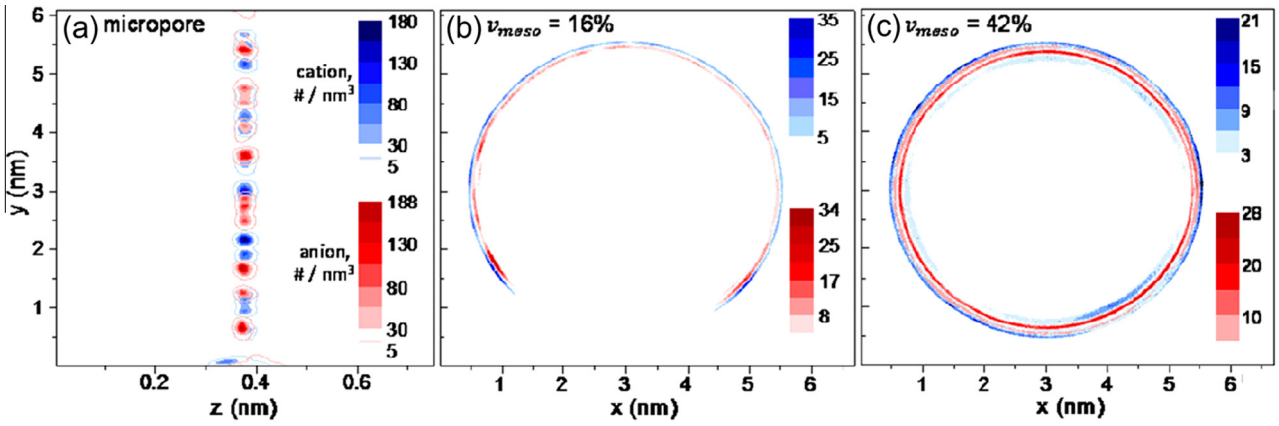

Fig. 9 – RTIL ion density along the pore wall direction. (a) The cation and anion density distributions along the length of the modeled slitlike micropore show a highly localized ion configuration, i.e. sharp maxima and clear co-ion separation with average separation of <1 nm. (b) and (c) Cross sectional view of the distributions through the modeled cylindrical mesopore at pore volume loadings v_{meso} = 16% (b) and 42% (c). The alternating ion structure perpendicular to the pore wall, plotted in Fig. 8a, is visible. Strong cation adsorption in (b) results in cation density maxima along the pore wall that are separated by ≈1 nm; the anion ordering follows a similar pattern in the next layer away from the wall. In (c), the competition between pore wall and intrinsic bulk interactions reduces the cation and anion sharp maxima along the wall and smears the distribution more evenly throughout the layers compared to in (b). The strong micropore wall–RTIL interaction that gives rise to the highly localized ions in (a) also reduces bulk-like interactions and allows some dynamic processes to occur faster than in the mesopore-confined (b and c) case.

to counter the influence of the surface and the density fluctuations are minimized.

Differences in the strength of the interaction potentials of RTIL ions with the mesopore walls (−154 kJ/mol) compared to with the micropore walls (−247 kJ/mol) contribute to the resulting RTIL structure within each confinement environment, which in turn affects the observed dynamics. The interaction potentials are obtained by calculating the net potential energy at the ions' equilibrium position between an ion pair and the carbon atoms of the pore wall. The considerably larger energy in the micropore case, then, is a consequence of having an additional wall in close proximity to the ions. A comparison of these interaction potentials with studies of the cohesive energy of $[C_4mim^+][Tf_2N^-]$ helps to explain the faster short-range motions inside the micropore. Estimates of the standard molar enthalpy of vaporization for this RTIL are between 136 kJ/mol and 174 kJ/mol [58], and due to a contact ion pair transitioning from the liquid phase to the gas phase. The cation–anion bond strength calculated for a single ion pair, however, is 305 kJ/mol [59]. These results suggest that (1) in the case of the bulk, mesopore-, and micropore-confined RTIL structures, all ions remain coordinated with at least their close-contact counterions, (2) the RTIL–micropore interaction disrupts the bulk RTIL structure to a greater extent than the RTIL–mesopore interaction, and (3) that the measured dynamics in S_1 are due to ions that are less coordinated than ions at the mesopore surface. The following analysis of the RTIL density fluctuations along the direction of the pore walls clearly illustrates these three points and helps explain the differences in the observed behavior between the different confinement environments.

In mesopores, RTIL ions are adsorbed to the surface, but still have significant coordination with the bulk-like fluid found away from the wall. We know from our previous study that diffusion along paths parallel to the cylinder surface is slower for paths closer to the pore wall than to the pore center [14]. Other studies have shown that the diffusion perpendicular to the pore wall is slower than parallel because the ions must traverse dense cation and anion layers [12]. The stronger the ordering, i.e., the higher the difference between density minima and maxima, the more difficult it is for the ions to penetrate the layers, and they are confined to cages formed by neighboring molecules for a longer time. Fig. 9 shows RTIL density fluctuations along the pore walls; the cation and anion densities are plotted along the length and width of the micropore (Fig. 9 a) and as cross-sections perpendicular to the mesopore cylinder axis (Fig. 9 b and c).

In the v_{meso} = 0.42 system (Fig. 9c), the cation and anion densities along the each respective layer show minimal change, indicating that RTIL motions along the layers encounter a relatively uniform resistance similar to the bulk liquid, but overall slower than the bulk due to the higher average ion density. In the v_{meso} = 0.16 system (Fig. 9b) the RTIL is less coordinated, mesopore surface effects dominate the RTIL structure and pronounced density maxima separated by ≈1 nm create barriers for diffusion along the layer direction. The density distributions, however, are spread out along the layer and minima between the high density regions are still observed. In the micropore (Fig. 9a), the RTIL is highly localized and co-ions are separated by <1 nm. Strong RTIL wall attraction, enhanced screening due to second wall at close proximity, a reduced excluded volume, and reduced coordination with the bulk structure all contribute to the resulting ion configuration. Fig. 9a shows that some RTIL ions are separated from other ions, forming islands. While long-range diffusion may be hindered by the presence of high density RTIL barriers,

the short length scale motions occurring within the neighbor molecule cages occur faster because the ions are less coordinated with other ions. This allows fluctuations in the average cation–anion separation and tail–tail conformational changes to occur unhindered by bulk interactions. We note that a recent computational study compared calculated self-diffusion of ionic liquid ions in charged narrow pores with that observed near charged planar surfaces and found that accelerated diffusion occurs to a higher extent in narrow pores [60]. In this study, they reasoned that it is because counter ions near charged surfaces are still bound to many co-ions in adjacent layers, and such binding disappears when ions form a monolayer inside a narrow pore. This reasoning is in line with the observations in this investigation.

4. Conclusion

This study provides molecular-level information of RTIL dynamics at an interface and inside micropores, an area that currently lacks sufficient experimental investigation in the EDLC community. The purpose of this study was to investigate the properties of the interfacial fluid in an electrode material whose hierarchical structure makes it a promising candidate for supercapacitor applications. One success of this study was to experimentally decouple the RTIL dynamics inside of micropores, which are completely filled in our system, from the better understood dynamics within a mesopore. The molecular-scale data we present provides a glimpse of the complex interactions at play and demonstrate the difficulty in defining all of the dynamics with a single parameter like diffusion.

Neutron spin echo spectroscopy and atomistic simulations were used in the current work to obtain quantitative information on the dynamics of RTIL electrolytes confined inside complex carbon electrode materials. The simple model, in which the measured properties were described as a linear combination of cylindrical mesopore and slit-like micropore effects, allows the molecular dynamics simulation to help describe RTIL [C_4mim^+][Tf_2N^-] dynamics inside a complex substrate. The confined RTIL exhibits fast relaxations occurring at times shorter than the current investigation, a primary relaxation component with time scales similar to the bulk, and a slow relaxation due to RTIL–pore wall interactions with a characteristic time scale several orders of magnitude slower. The MD simulations find agreement with the NSE data only after considering the micropore effects. It was found that a significant fraction of RTIL interacts with the pore walls and is effectively immobilized, with long relaxation times outside the current measurement's range, yet estimated to be on the 100 ns timescale at high temperature.

This work shows that both the influence of the bulk fluid and the RTIL–wall interactions must be considered and the overall motions of the ions will be the net result of both effects. While the dynamics near a smooth mesopore carbon surface are slower than in the bulk phase, this study finds that some RTIL ions inside of micropores with ideal flat walls are less coordinated than those in the bulk liquid and exhibit faster collective motions on length scales of the ion separation than RTIL at the mesopore surface (RTIL at a mesopore wall is still in contact with bulk-like RTIL). Recent work has discussed the complex dynamic features of RTILs at interfaces, including the extent to which RTIL dissociation may occur [61–63]. The experiment and modeling approach presented in this work offers new information on the dynamics of RTIL confined in two distinct pore geometries. This work has shown that confined RTIL dynamics depend on the confining geometry, temperature affects to what extent RTIL is immobilized at the surface, and RTIL density fluctuations affect collective ion motions along perpendicular and parallel paths to the confining surfaces in similar ways. These fluctuations slow down long-range diffusion, but allow faster motions on the length scale of the ion separation distance.

The current observations may shed light on how high electrical double layer capacitance [64] is achieved in hierarchical microporous–mesoporous carbons for use in energy storage devices [6]. Though it is true that the micropores offer high surface area for energy storage and materials are typically designed with open mesoporous "highways" for efficient ion transport, not much is known about the dynamics of ions in micropores, that is, pores whose dimensions nearly match the size of the RTIL molecules. It is conceivable that other micropore sizes could allow more bulk-like interactions and that the fast micropore motions would be slower than in the mesopore. One emerging observation in the EDLC community is that capacitance exhibits oscillatory behavior as a function of pore-size, when the pores are less than to several ion diameters in size. Establishing a connection between this observation and the mobility of ions in pores of similar dimensions may help explain why desirable properties in supercapacitors are obtained when pore size is chosen carefully with respect to a given electrolyte [65], and is an area that requires further study. It has been recently shown that fast charging of micropores is a process aided by fast ion diffusion (by an order of magnitude compared to bulk), that charging is accelerated by collective modes, and that charging is highly dependent on the geometry and chemistry of the system [60]. Similar to our observations, the behavior was ascribed to lower level of coordination with the bulk fluid when the RTIL is confined in micropores. An in-depth systematic study would be necessary to understand the relation between the current work and these recent findings, but both suggest a re-evaluation of the nanopore-scale factors responsible for EDLC behavior.

Disclaimer

The full description of the procedures used in this paper requires the identification of certain commercial products and their suppliers. The inclusion of such information should in no way be construed as indicating that such products or suppliers are endorsed by NIST or are recommended by NIST or that they are necessarily the best materials, instruments, software or suppliers for the purposes described.

Acknowledgments

This work was supported as part of the Fluid Interface Reactions, Structures and Transport (FIRST) Center, an Energy

Frontier Research Center funded by the U.S. Department of Energy, Office of Science, Office of Basic Energy Sciences. The SNS NSE portion and bulk liquid diffraction portion of this research conducted at Oak Ridge National Laboratory's Spallation Neutron Source was sponsored by the Scientific User Facilities Division, Office of Basic Energy Sciences, U.S. Department of Energy. The NIST NSE portion of this work utilized facilities supported in part by the National Science Foundation under Agreement No. DMR-0944772. G.F. thanks the Palmetto Cluster at Clemson University for providing computational resources. The authors thank the reviewers for their insightful comments that helped improve the clarity and strengthen certain points in this work. The authors would like to acknowledge M. Monkenbusch of the Jülich Centre for Neutron Science JCNS for his helpful discussions during the SNS NSE experiment, review of the manuscript, and helpful comments. The authors acknowledge C. Liao, formerly of Oak Ridge National Laboratory (ORNL) for performing the anion exchange in the deuterated RTIL, as well as X. Wang, formerly of ORNL, for the synthesis of the 5.8 nm-confined RTIL compound. The authors also acknowledge T. Kozielewski and M. Ohl of JCNS Outstation at SNS for their assistance in setting up the NSE experiments on BL-15 at the SNS, as well as C. Do of ORNL for assistance during beam time on BL-6B at the SNS.

REFERENCES

[1] Armand M, Endres F, MacFarlane DR, Ohno H, Scrosati B. Ionic-liquid materials for the electrochemical challenges of the future. Nat Mater 2009;8(8):621–9.
[2] Castner EW, Wishart JF. Spotlight on ionic liquids. J Chem Phys 2010;132(12):120901-1–9.
[3] Ohno H. Electrochemical aspects of ionic liquids. New York: Wiley-Interscience; 2005.
[4] Simon P, Gogotsi Y. Materials for electrochemical capacitors. Nat Mater 2008;7(11):845–54.
[5] Inagaki M, Konno H, Tanaike O. Carbon materials for electrochemical capacitors. J Power Sources 2010;195(24):7880–903.
[6] Zhai Y, Dou Y, Zhao D, Fulvio PF, Mayes RT, Dai S. Carbon materials for chemical capacitive energy storage. Adv Mater 2011;23(42):4828–50.
[7] Kofu M, Nagao M, Ueki T, Kitazawa Y, Nakamura Y, Sawamura S, et al. Heterogeneous slow dynamics of imidazolium-based ionic liquids studied by neutron spin echo. J Phys Chem B 2013;117(9):2773–81.
[8] Yamaguchi T, Mikawa K-I, Koda S, Fujii K, Endo H, Shibayama M, et al. Relationship between mesoscale dynamics and shear relaxation of ionic liquids with long alkyl chain. J Chem Phys 2012;137(10):104511–7.
[9] Yamamuro O, Yamada T, Kofu M, Nakakoshi M, Nagao M. Hierarchical structure and dynamics of an ionic liquid 1-octyl-3-methylimidazolium chloride. J Chem Phys 2011;135:054508-1–7 [1089-7690 (Electronic)].
[10] Russina O, Beiner M, Pappas C, Russina M, Arrighi V, Unruh T, et al. Temperature dependence of the primary relaxation in 1-hexyl-3-methylimidazolium bis{(trifluoromethyl)sulfonyl}imide. J Phys Chem B 2009;113(25):8469–74.
[11] Sarangi SS, Zhao W, Muller-Plathe F, Balasubramanian S. Correlation between dynamic heterogeneity and local structure in a room-temperature ionic liquid: a molecular dynamics study of bmim PF(6). ChemPhysChem 2010;11(9):2001–10.
[12] Singh R, Monk J, Hung FR. Heterogeneity in the dynamics of the ionic liquid [BMIM$^+$][PF6$^-$] confined in a slit nanopore. J Phys Chem C 2011;115(33):16544–54.
[13] Coasne B, Viau L, Vioux A. Loading-controlled stiffening in nanoconfined ionic liquids. J Phys Chem Lett 2011;2(10):1150–4.
[14] Li S, Han KS, Feng G, Hagaman EW, Vlcek L, Cummings PT. Dynamic and structural properties of room-temperature ionic liquids near silica and carbon surfaces. Langmuir 2013;29(31):9744–9.
[15] Kornyshev AA. Double-layer in ionic liquids: paradigm change? J Phys Chem B 2007;111(20):5545–57.
[16] Wu J, Jiang T, Jiang D-E, Jin Z, Henderson D. A classical density functional theory for interfacial layering of ionic liquids. Soft Matter 2011;7(23):11222–31.
[17] Black JM, Walters D, Labuda A, Feng G, Hillesheim PC, Dai S, et al. Bias-dependent molecular-level structure of electrical double layer in ionic liquid on graphite. Nano Lett 2013;13(12):5954–60.
[18] Zhou H, Rouha M, Feng G, Lee SS, Docherty H, Fenter P, et al. Nanoscale perturbations of room temperature ionic liquid structure at charged and uncharged interfaces. ACS Nano 2012;6(11):9818–27.
[19] Perkin S. Ionic liquids in confined geometries. Phys Chem Chem Phys 2012;14(15):5052–62.
[20] Bañuelos JL, Feng G, Fulvio PF, Li S, Rother G, Dai S, et al. Densification of ionic liquid molecules within a hierarchical nanoporous carbon structure revealed by small-angle scattering and molecular dynamics simulation. Chem Mater 2014;26(2):1144–53.
[21] Jobic H, Methivier A, Ehlers G, Farago B, Haeussler W. Accelerated diffusion of long-chain alkanes between nanosized cavities. Angew Chem Int Ed 2004;43(3):364–6.
[22] Swenson J, Bergman R, Longeville S. A neutron spin-echo study of confined water. J Chem Phys 2001;115(24):11299–305.
[23] Kusmin A, Gruener S, Henschel A, de Souza N, Allgaier Jr, Richter D, et al. Polymer dynamics in nanochannels of porous silicon: a neutron spin echo study. Macromolecules 2010;43(19):8162–9.
[24] Kusmin A, Gruener S, Henschel A, Holderer O, Allgaier J, Richter D, et al. Evidence of a sticky boundary layer in nanochannels: a neutron spin echo study of n-hexatriacontane and poly(ethylene oxide) confined in porous silicon. J Phys Chem Lett 2010;1(20):3116–21.
[25] Martín J, Krutyeva M, Monkenbusch M, Arbe A, Allgaier J, Radulescu A, et al. Direct observation of confined single chain dynamics by neutron scattering. Phys Rev Lett 2010;104(19):197801.
[26] Krutyeva M, Wischnewski A, Monkenbusch M, Willner L, Maiz J, Mijangos C, et al. Effect of nanoconfinement on polymer dynamics: surface layers and interphases. Phys Rev Lett 2013;110(10):108303.
[27] Wang X, Liang C, Dai S. Facile synthesis of ordered mesoporous carbons with high thermal stability by self-assembly of resorcinol–formaldehyde and block copolymers under highly acidic conditions. Langmuir 2008;24(14):7500–5.
[28] Tokuda H, Hayamizu K, Ishii K, Susan M, Watanabe M. Physicochemical properties and structures of room temperature ionic liquids. 2. Variation of alkyl chain length in imidazolium cation. J Phys Chem B 2005;109(13):6103–10.
[29] Fredlake CP, Crosthwaite JM, Hert DG, Aki SNVK, Brennecke JF. Thermophysical properties of imidazolium-based ionic liquids. J Chem Eng Data 2004;49(4):954–64.
[30] Liu H, Maginn E. A molecular dynamics investigation of the structural and dynamic properties of the ionic liquid 1-n-

butyl-3-methylimidazolium bis(trifluoromethanesulfonyl)imide. J Chem Phys 2011;135(12):124507–16.
[31] Russina O, Triolo A, Gontrani L, Caminiti R, Xiao D, Hines LG, et al. Morphology and intermolecular dynamics of 1-alkyl-3-methylimidazolium bis{(trifluoromethane)sulfonyl}amide ionic liquids: structural and dynamic evidence of nanoscale segregation. J Phys: Condens Matter 2009;21(42):1–9.
[32] Bodo E, Gontrani L, Caminiti R, Plechkova NV, Seddon KR, Triolo A. Structural properties of 1-alkyl-3-methylimidazolium bis{(trifluoromethyl)sulfonyl}amide ionic liquids: X-ray diffraction data and molecular dynamics simulations. J Phys Chem B 2010;114(49):16398–407.
[33] Köddermann T, Paschek D, Ludwig R. Molecular dynamic simulations of ionic liquids: a reliable description of structure, thermodynamics and dynamics. ChemPhysChem 2007;8(17):2464–70.
[34] Zhao W, Eslami H, Cavalcanti WL, Müller-Plathe F. A refined all-atom model for the ionic liquid 1-n-butyl 3-methylimidazolium bis(trifluoromethylsulfonyl)imide [Bmim][Tf2N]. Z Phys Chem 2007;221(11–12):1647–62.
[35] Sing KSW, Everett DH, Haul RAW, Mouscou L, Pierotti RA, Rouquerol J, et al. Reporting physisorption data for gas/solid systems. Pure Appl Chem 1985;57(4):603–19.
[36] Maginn EJ. Molecular simulation of ionic liquids: current status and future opportunities. J Phys: Condens Matter 2009;21(37):1–17.
[37] Maginn EJ. Atomistic simulation of the thermodynamic and transport properties of ionic liquids. Acc Chem Res 2007;40(11):1200–7.
[38] Fulvio PF, Mayes RT, Wang X, Mahurin SM, Bauer JC, Presser V, et al. "Brick-and-mortar" self-assembly approach to graphitic mesoporous carbon nanocomposites. Adv Funct Mater 2011;21(12):2208–15.
[39] Wang XQ, Liang CD, Dai S. Facile synthesis of ordered mesoporous carbons with high thermal stability by self-assembly of resorcinol-formaldehyde and block copolymers under highly acidic conditions. Langmuir 2008;24(14):7500–5.
[40] Burrell AK, Sesto RED, Baker SN, McCleskey TM, Baker GA. The large scale synthesis of pure imidazolium and pyrrolidinium ionic liquids. Green Chem 2007;9(5):449–54.
[41] Jaroniec M, Solovyov LA. Improvement of the Kruk–Jaroniec–Sayari method for pore size analysis of ordered silicas with cylindrical mesopores. Langmuir 2006;22(16):6757–60.
[42] Choma J, Górka J, Jaroniec M. Mesoporous carbons synthesized by soft-templating method: determination of pore size distribution from argon and nitrogen adsorption isotherms. Microporous Mesoporous Mater 2008;112(1–3):573–9.
[43] Kruk M, Jaroniec M, Gadkaree KP. Nitrogen adsorption studies of novel synthetic active carbons. J Colloid Interface Sci 1997;192(1):250–6.
[44] Squires GL. Introduction to the theory of thermal neutron scattering. Mineola, NY: Dover; 1996. p. 260.
[45] Guinier A. X-ray diffraction in crystals, imperfect crystals, and amorphous bodies. New York: Dover Publications; 1963.
[46] Gomes de Azevedo R, Esperança JMSS, Szydlowski J, Visak ZP, Pires PF, Guedes HJR, et al. Thermophysical and thermodynamic properties of ionic liquids over an extended pressure range: [bmim][NTf2] and [hmim][NTf2]. J Chem Thermodyn 2005;37(9):888–99.
[47] Azuah RT, Kneller LR, Qiu Y, Tregenna-Piggott PLW, Brown CM, Copley JRD, et al. DAVE: a comprehensive software suite for the reduction, visualization, and analysis of low energy neutron spectroscopic data. J Res Nat Inst Stand Technol 2009;114(6):341–58.
[48] Ohl M, Monkenbusch M, Arend N, Kozielewski T, Vehres G, Tiemann C, et al. The spin-echo spectrometer at the Spallation Neutron Source (SNS). Nucl Instrum Methods A 2012;696:85–99.
[49] Rosov N, Rathgeber S, Monkenbusch M, Neutron spin echo spectroscopy at the NIST Center for Neutron Research. In: Cebe P, Hsiao BS, Lohse DJ, editors. Scattering from polymers: characterization by X-rays, neutrons, and light. ACS symp. ser. vol. 739. Washington, DC; 2000. p. 103–16.
[50] Zhao JK, Gao CY, Liu D. The extended Q-range small-angle neutron scattering diffractometer at the SNS. J Appl Crystallogr 2010;43(5):1068–77.
[51] Annapureddy HVR, Kashyap HK, De Biase PM, Margulis CJ. What is the origin of the prepeak in the X-ray scattering of imidazolium-based room-temperature ionic liquids? J Phys Chem B 2010;114(50):16838–46.
[52] Mamontov E, Luo HM, Dai S. Proton dynamics in N,N,N′,N′-tetramethylguanidinium bis(perfluoroethylsulfonyl)imide protic ionic liquid probed by quasielastic neutron scattering. J Phys Chem B 2009;113(1):159–69.
[53] Mamontov EME, Baker GA, Luo HM, Dai S. Microscopic diffusion dynamics of silver complex-based room-temperature ionic liquids probed by quasielastic neutron scattering. ChemPhysChem 2011;12(5):944–50.
[54] Chathoth SM, Mamontov E, Dai S, Wang X, Fulvio PF, Wesolowski DJ. Fast diffusion in a room temperature ionic liquid confined in mesoporous carbon. EPL (Europhys. Lett.) 2012;97(6):66004.
[55] Róg T, Murzyn K, Hinsen K, Kneller GR. NMoldyn: a program package for a neutron scattering oriented analysis of molecular dynamics simulations. J Comput Chem 2003;24(5):657–67.
[56] Gennes PGD. Liquid dynamics and inelastic scattering of neutrons. Physica 1959;25:825–39.
[57] Li S, Bañuelos JL, Guo J, Anovitz L, Rother G, Shaw RW, et al. Alkyl chain length and temperature effects on structural properties of pyrrolidinium-based ionic liquids: a combined atomistic simulation and small-angle X-ray scattering study. J Phys Chem Lett 2012;3(1):125–30.
[58] Kelkar MS, Maginn EJ. Calculating the enthalpy of vaporization for ionic liquid clusters. J Phys Chem B 2007;111(32):9424–7.
[59] Fernandes AM, Rocha MAA, Freire MG, Marrucho IM, Coutinho JoAP, Santos LsMNBF. Evaluation of cation–anion interaction strength in ionic liquids. J Phys Chem B 2011;115(14):4033–41.
[60] Kondrat S, Wu P, Qiao R, Kornyshev AA. Accelerating charging dynamics in subnanometre pores. Nat Mater 2014;13(4):387–93.
[61] Gebbie MA, Valtiner M, Banquy X, Fox ET, Henderson WA, Israelachvili JN. Ionic liquids behave as dilute electrolyte solutions. Proc Natl Acad Sci 2013;110(24):9674–9.
[62] Perkin S, Salanne M, Madden P, Lynden-Bell R. Is a Stern and diffuse layer model appropriate to ionic liquids at surfaces? Proc Natl Acad Sci 2013;110(44). E4121.
[63] Gebbie MA, Valtiner M, Banquy X, Henderson WA, Israelachvili JN. Reply to Perkin et al.: experimental observations demonstrate that ionic liquids form both bound (Stern) and diffuse electric double layers. Proc Natl Acad Sci 2013;110(44):E4122.
[64] Feng G, Li S, Presser V, Cummings PT. Molecular insights into carbon supercapacitors based on room-temperature ionic liquids. J Phys Chem Lett 2013:3367–76.
[65] Chmiola J, Yushin G, Gogotsi Y, Portet C, Simon P, Taberna PL. Anomalous increase in carbon capacitance at pore sizes less than 1 nanometer. Science 2006;313(5794):1760–3.